Proceedings of the
Annual Stability Conference
Structural Stability Research Council
St. Louis, Missouri, April 16-20, 2013

Distortional Buckling Capacity of Z-Purlins Through-Fastened to Metal Panels under Gravity Loading

C.N.Grey[1], C.D. Moen[2], P.G.Cranston[3]

Abstract
The governing limit state for cold-formed steel purlins used in a metal building can be distortional buckling, where the compressed flange in contact with corrugated metal roof panels deforms in up-down half-waves along the length of the member. Current code equations for calculating distortional buckling capacity were derived experimentally with four-point bending tests; however, the controlling gravity load case for roof purlins can be snow or wind that may suppress these distortional buckling half-waves. This paper presents an experimental and computational study to explore and quantify the distortional buckling flexural capacity of metal building Zee purlins with and without through-fastened panels considering both four-point bending and a uniform pressure applied to the metal roof panels. A total of 12 tests were conducted on a typical metal building roof system employing a vacuum chamber, the results of which are compared to AISI Direct Strength Method capacity predictions. A thin-shell finite element modeling protocol for a metal building roof system, including contact effects and the individual screw fasteners, is presented and validated with the experiments. The protocol is used to study and explain the complicated distortional buckling panel-purlin interaction for the downward pressure load case.

[1] Staff I – Building Technology, Simpson Gumpertz & Heger Inc., <cngrey@sgh.com>
[2] Assistant Professor, Civil & Environmental Engineering, Virginia Polytechnic Institute and State University, <cmoen@vt.edu>
[3] Staff II – Structures, Simpson Gumpertz & Heger Inc., <pgcranston@sgh.com>

1. Introduction

Through-fastened metal building roof systems are constructed with corrugated roofing panels attached to cold-formed steel Zee or Cee purlins with self-tapping screws. The purlin compression flange is assumed to be fully braced by the through-fastened roof. Purlin flexural capacity predictions are calculated with the AISI Direct Strength Method (DSM) (AISI-S100 2007) employing the local and distortional elastic buckling parameters from a finite strip analysis (Schafer and Adany 2006) and the flexural yield strength. Recent research has demonstrated that rotational restraint provided to the compression flange by means of a through-fastened metal deck can boost distortional buckling capacity (Schafer and Yu 2006, Schafer et al. 2008). These experiments were conducted with four-point bending; however, a uniform pressure loading is the more-realistic loading condition, e.g., a snow loading. It has been hypothesized that downward uniform pressure improves distortional buckling capacity by preventing the upward half-waves from forming. The goal of the research described herein is to evaluate the viability of this hypothesis.

2. Experimental Program

2.1 Rationale for cross-section selection

A Zee cross-section was chosen with a predicted distortional buckling capacity lower than local and local-global buckling interaction limit states as shown in Figure 1. The selected cross-section is an 8.5 in. web (h), 2.5 in. flange (b_c), and 0.079 in. thickness (t) Zee section with additional dimensions summarized in Figure 2. Midspan bracing is provided to prevent lateral-torsional buckling for tests where the panel in not attached. Bracing locations were determined by increasing the midspan unbraced distance to a point where at least three distortional buckling half-waves (measured from elastic buckling curve in Figure 1) could form but still adequately prevent lateral-torsional buckling (Figure 3). An initial DSM unrestrained capacity calculation summarized in Table 1 demonstrates that the distortional buckling limit state will control in the tests.

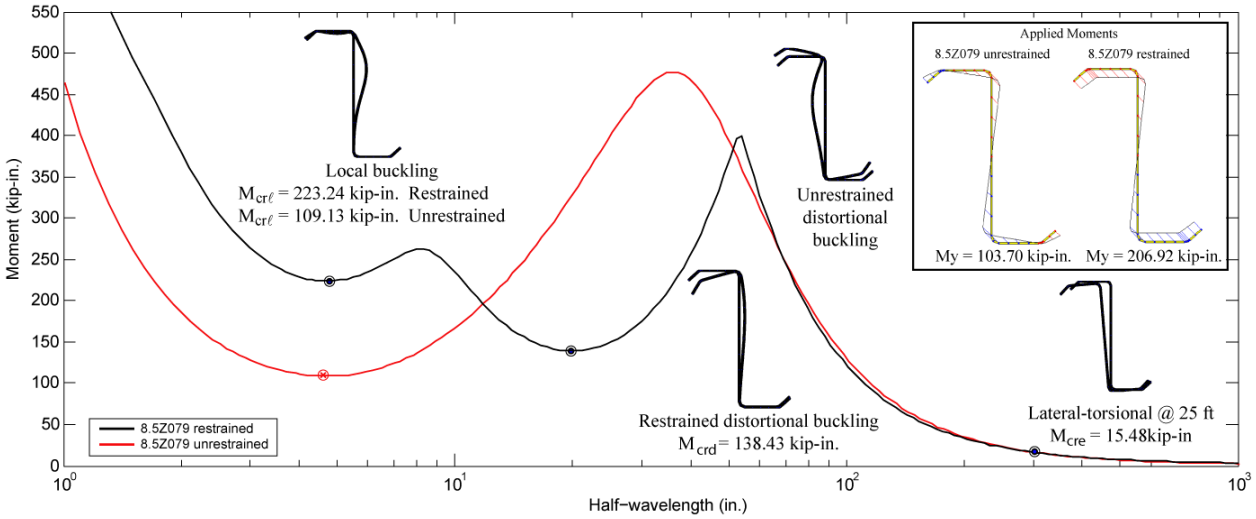

Figure 1: Cold-formed steel beam Zee section elastic buckling modes.

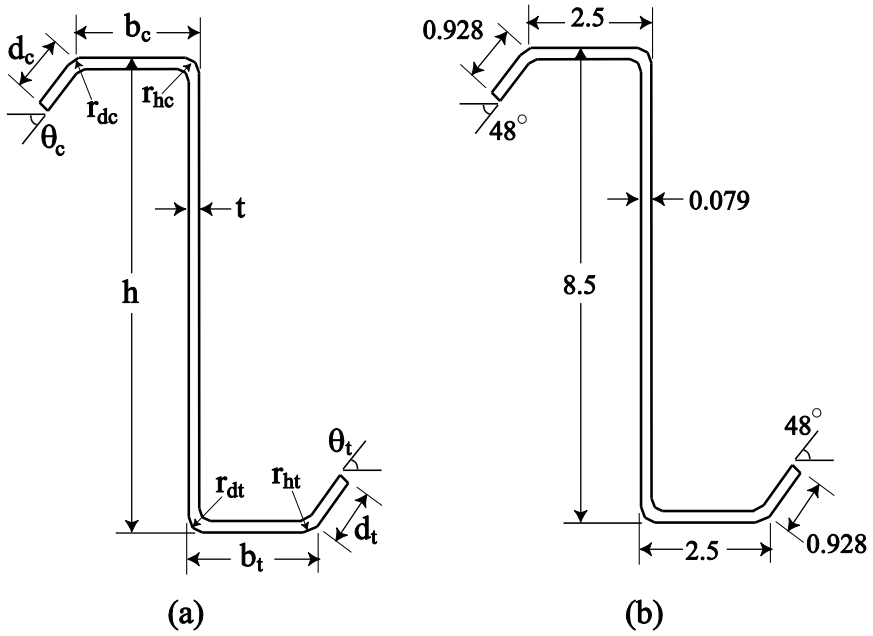

Figure 2: (a) Cross-section dimension notation and (b) nominal dimensions (in.).

Table 1: Nominal capacity prediction.

	Elastic Buckling Properties				Direct Strength Method						
	Yield	Unrestrained Bending			Global	Local		Distortional		Nominal	
Section	$M_{y,u}$ (kip-in.)	$M_{cr\ell,u}$ (kip-in.)	$M_{crd,u}$ (kip-in.)	$M_{cre,u}$ (kip-in.)	M_{ne} (kip-in.)	λ_ℓ	$M_{n\ell}$ (kip-in.)	λ_d	M_{nd} (kip-in.)	$M_{n,DSM}$ (kip-in.)	Controlling Mode
8.5Z079	103.7	109.13	109.13	194.61	98.17	0.95	86.40	0.97	82.37	82.37	(distortional controls)

2.2 Test setup

Each test specimen is constructed with two parallel simply supported (pin-roller) Zee purlins spaced at 5 ft on center to the center of the web. The purlins are oriented in opposing directions to equilibrate the tendency of the purlin to roll laterally about its weak principal axis when the paneling is attached. A 1.25 in. deep corrugated roofing panel (t = 0.018 in.) spans between purlins with a 1 ft overhang (measured from the center of the web) and is attached to the purlins with 2-1/2 in. self-tapping screws spacing at 12 in. on center. Connectivity between purlins is achieved with hot-rolled tube sections, 2 x 5 x 0.375 in., welded to a 6 x 6 x 0.375 in. plate bolted to the webs at the support and at the intermediate points as shown in Figure 3. Bracing provides full web restraint at the supports and loading locations.

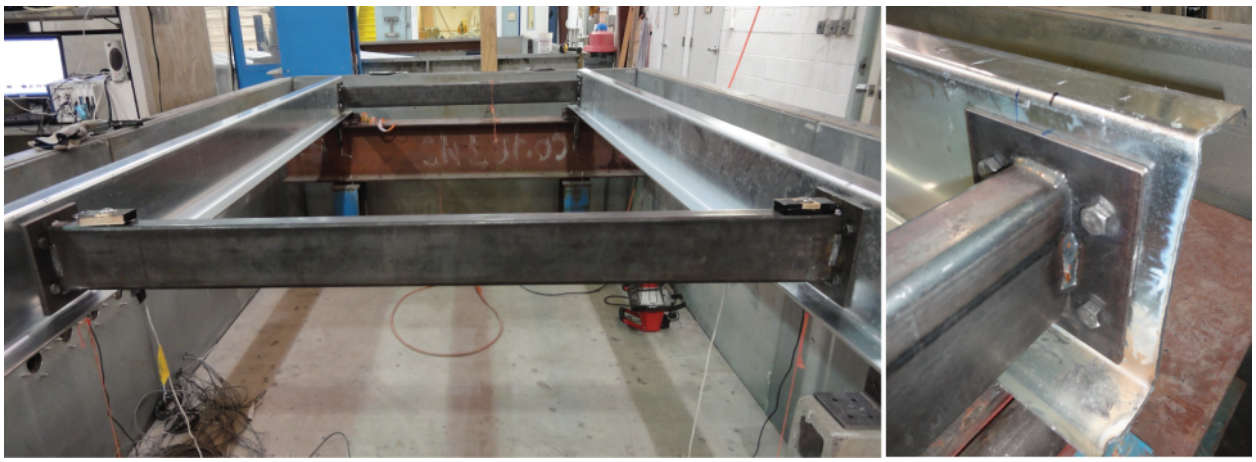

Figure 3: Bracing provided for lateral-torsional buckling prevention.

The three testing scenarios designed to quantify the influence of downward pressure are presented in Figure 5 with specific information about each test provided in Table 2. The first testing scenario (Figure 5a, UB-P) follows the standard base test method for purlins supporting standing-seam roof systems, AISI S908-08 (AISI-TS 2007), which simulates uniform bending from a downward pressure. The through-fastened roof system is sealed in the chamber with plastic, and air is pulled from the chamber with a series of vacuum pumps. Load (negative pressure) is increased by closing multiple outflow valves at a controlled rate.

The second test configuration (Figure 5b, 4PB-P) uses a loading frame (Figure 4) inside the pressure chamber (box) to apply four-point bending to the purlins (panel included). The chamber is sealed with plastic, and a negative pressure is applied. The loading frame transforms the pressure loading into four-point bending. Load cells are placed at the loading points (Figure 4). The four-point bending test is performed inside the chamber to ensure that the boundary conditions are consistent between test types. Comparing the four-point bending tests to the downward pressure tests described previously isolates the influence of downward gravity pressure on system capacity.

The third test type (4PB-NP) also uses the loading frame shown in Figure 5b to apply four-point bending with a negative pressure, except for these specimens, the through-fastened panel has been removed. This test configuration isolates the contribution of the panel to distortional buckling capacity.

Figure 4: Loading frame and load cells.

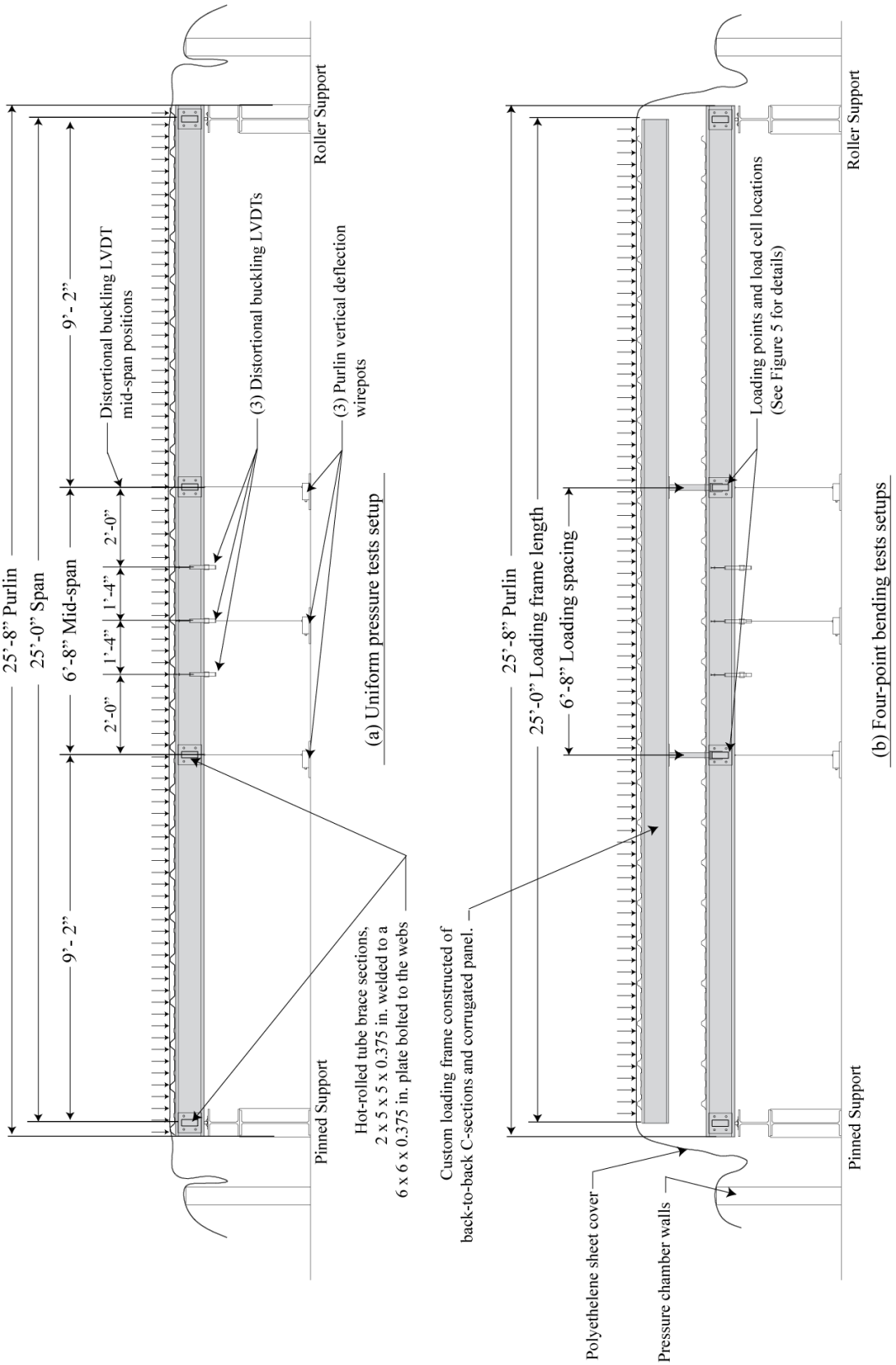

Figure 5: Elevation views of test setups.

Table 2: Measured cross-section dimensions.

Test Label	Purlin Label	h (in)	b_c (in)	$b_{c\,(flat)}$ (in)	d_c (in)	$d_{c(flat)}$ (in)	θ_c (deg)	r_{hc} (in)	r_{dc} (in)	b_t (in)	$b_{t(flat)}$ (in)	d_t (in)	$d_{t(flat)}$ (in)	θ_t (deg)	r_{ht} (in)	r_{dt} (in)	t (in)	f_y (ksi)
UB-P-1-24E25W	24	8.371	2.424	1.956	0.821	0.683	53	0.254	0.385	2.644	1.955	0.902	0.648	56	0.321	0.543	0.081	72.56
	25	8.391	2.518	1.876	0.856	0.674	47	0.279	0.513	2.590	1.884	0.955	0.764	53	0.453	0.366	0.081	72.61
UB-P-2-22E23W	22	8.373	2.389	2.069	0.808	0.704	52	0.271	0.535	2.490	1.999	0.822	0.496	53	0.241	0.447	0.080	72.25
	23	8.403	2.240	2.044	0.808	0.624	47	0.291	0.467	2.325	2.046	0.937	0.708	53	0.232	0.489	0.081	72.13
UB-P-3-12E13W	12	8.224	2.238	2.008	0.768	0.648	45	0.175	0.303	2.617	2.027	0.833	0.499	55	0.284	0.587	0.082	71.83
	13	8.196	2.574	2.084	0.928	0.705	53	0.288	0.447	2.495	2.129	0.764	0.625	45	0.205	0.338	0.079	71.68
4PB-P-1-16E14W	16	8.221	2.518	1.913	0.813	0.619	47	0.338	0.504	2.558	2.136	0.841	0.701	53	0.197	0.486	0.080	72.21
	14	8.214	2.424	2.018	0.816	0.667	55	0.254	0.373	2.544	2.087	0.836	0.603	46	0.194	0.453	0.080	71.97
4PB-P-2-19E11W	19	8.185	2.629	2.124	0.955	0.703	52	0.255	0.597	2.316	1.923	0.816	0.637	46	0.143	0.420	0.081	71.61
	11	8.241	2.588	2.122	0.980	0.782	52	0.219	0.426	2.499	2.058	0.770	0.594	47	0.218	0.445	0.080	72.25
4PB-P-3-21E7W	21	8.295	2.540	2.187	0.879	0.607	53	0.270	0.550	2.550	2.084	0.794	0.529	45	0.234	0.540	0.081	72.40
	7	8.237	2.329	2.001	0.783	0.596	54	0.246	0.678	2.359	1.996	0.840	0.672	44	0.243	0.522	0.081	72.38
4PB-NP-1-15E8W	15	8.254	2.444	1.987	0.787	0.633	46	0.268	0.378	2.568	2.111	0.709	0.520	53	0.184	0.415	0.081	71.83
	8	8.324	2.599	2.050	0.933	0.707	53	0.293	0.473	2.454	2.000	0.881	0.758	47	0.233	0.375	0.080	73.00
4PB-NP-2-10E9W	10	8.201	2.458	1.985	0.836	0.669	50	0.184	0.409	2.553	2.153	0.910	0.726	53	0.217	0.484	0.079	71.67
	9	8.216	2.622	2.063	0.963	0.686	53	0.274	0.592	2.446	2.063	0.747	0.582	46	0.138	0.405	0.080	72.18
4PB-NP-3-17E18W	17	8.267	2.386	1.846	0.789	0.585	44	0.267	0.632	2.675	2.070	1.029	0.819	52	0.283	0.502	0.087	74.46
	18	8.250	2.535	2.072	0.808	0.567	55	0.313	0.581	2.388	1.964	0.713	0.546	47	0.313	0.527	0.088	73.60
4PB-NP-4-32E20W	32	8.304	2.452	2.085	1.061	0.869	51	0.170	0.522	2.426	1.917	0.876	0.687	48	0.318	0.457	0.080	75.89
	20	8.215	2.483	2.136	0.765	0.634	52	0.293	0.608	2.415	2.001	0.895	0.549	45	0.176	0.498	0.080	71.54

Note: Typical test label is xx-x-x-xxxx.

For example, test 4PB-NP-2-8E15W means Four-point Bending No Panel Test 2
with the paired specimens 8.5Z079-8 on the east side and 8.5Z079-15 on the west side

2.3 Instrumentation

All data acquisition is managed using the commercially available National Instruments (NI) PXI-1052 Data Acquisition system managed by NI Labview graphical environment software. Labview allows the user to monitor all instrumentation on one screen as the test is being conducted. All instrumentation is calibrated using NI Automation and Measurement software.

Pressure transducers with a range of 0 – 2,160 psf accurate to +/- 0.1 psf are positioned at each end of the chamber to ensure that loading is consistent throughout the chamber. Wire pot displacement transducers with a range of +/- 5 in. and an accuracy of +/- 0.01 in. were used to record vertical purlin deflection at midspan and load (brace) points. To detect the formation of distortional buckling half-wavelengths, linear variable differential transducers (LVDTs) with a range of +/- 3 in. and an accuracy of +/- 0.001 in. were placed at midspan at three locations dimensioned in Figure 5 and shown in Figure 6. The information from these transducers is used to measure the magnitude of distortional buckling as well as half-wavelength directionality. The first test, UB-P-1, does not have any distortional buckling data, as it was used to determine positioning of the LVDTs at the half-wavelength maximums. To ensure that equal loading is applied to the purlin system during the 4PB-P and 4PB-NP tests, a load cell with a range of 0 – 10 kip and accuracy of +/- 0.001 kip was positioned at each load point.

Figure 6: Distortional buckling LVDTs.

2.4 Specimen measurements

The cross-section dimensions were measured at the midlength of each purlin and are summarized in Table 2. Each purlin was clamped down over two sawhorses. The profile of the purlin was transferred to engineering paper using a 6.0 in. contour gauge, and radii, flange widths, lip lengths, and angles were measured using a digital caliper accurate to +/- 0.001 in. Radii, flange widths, lip lengths, and angles were measured using this method.

2.5 Material properties

Tensile coupon tests were performed on all specimens using ASTM A370-05 (ASTM 2005). Three tensile coupons were taken from a 1 ft untested section at the end of each specimen: one coupon each from the compression flange, tension flange, and web. Sharp yielding stress results are reported as the average of the three coupons in Table 2, with an average across all specimens of 72.5 ksi.

3. Elastic Buckling and DSM Strength Prediction

The critical elastic restrained and unrestrained buckling moments for local ($M_{cr\ell}$), distortional (M_{crd}), and global (M_{cre}) were obtained with a finite strip analysis and measured specimen cross-section dimensions in CUFSM (Schafer and Ádány 2006) presented in Table 3. Note that the finite strip method predicts no distinctive distortional buckling mode, as there is modal interaction with local buckling. This is due to the stiffener lip being in tension which braces the flange and $M_{cr\ell,u}$ and $M_{crd,u}$ are taken to be the same. Presented are all elastic buckling parameters for the measured cross-section properties in Table 2 along with yield moments using CUFSM. The global buckling moment is reported as M_{cre} and is taken at an unbraced length equal to the distance between the braces as discussed previously.

Table 3: Elastic buckling results.

Test Label	Purlin Label	Finite Strip Method (CUFSM)							
		Yield Moment		Restrained Bending			Unrestrained Bending		
		$M_{y,r}$ (kip-in.)	$M_{y,u}$ (kip-in.)	$M_{cr\ell,r}$ (kip-in.)	$M_{crd,r}$ (kip-in.)	$M_{cre,r}$ (kip-in.)	$M_{cr\ell,u}$ (kip-in.)	$M_{crd,u}$ (kip-in.)	$M_{cre,u}$ (kip-in.)
UB-P-1-24E25W	24	211.79	106.59	228.22	167.60	168.83	118.93	118.93	172.96
	25	211.70	106.77	230.29	156.08	170.50	118.24	118.24	174.88
UB-P-2-22E23W	22	206.93	104.44	238.37	160.86	205.96	107.50	107.50	214.55
	23	215.80	106.83	232.40	146.99	184.13	117.33	117.33	190.91
UB-P-3-12E13W	12	203.25	102.56	229.31	146.37	147.54	123.68	123.68	151.04
	13	200.72	100.03	228.60	156.60	192.31	105.78	105.78	200.82
4PB-P-1-16E14W	16	204.70	101.17	224.50	143.48	168.44	116.26	116.26	174.47
	14	203.66	100.54	226.51	161.63	168.03	111.38	111.38	173.95
4PB-P-2-19E11W	19	199.06	101.57	254.29	163.23	216.01	110.67	110.67	229.08
	11	206.29	102.42	236.90	164.30	199.98	109.95	109.95	208.23
4PB-P-3-21E7W	21	213.09	105.81	246.23	154.93	212.36	113.23	113.23	223.09
	7	210.48	104.69	243.46	165.49	198.52	115.62	115.62	206.74
4PB-NP-1-15E8W	15	203.95	101.25	230.17	142.63	160.05	114.47	114.47	166.10
	8	211.70	105.89	234.20	162.36	197.15	110.60	110.60	205.21
4PB-NP-2-10E9W	10	199.22	99.53	208.72	149.14	155.68	113.82	113.82	159.13
	9	202.24	102.14	242.21	161.89	207.35	107.81	107.81	217.68
4PB-NP-3-17E18W	17	228.22	115.27	276.08	167.71	172.41	152.75	152.75	177.34
	18	229.76	114.17	314.38	191.29	217.09	145.17	145.17	229.51
4PB-NP-4-32E20W	32	219.01	109.26	240.04	172.71	215.63	110.99	110.99	222.88
	20	200.86	101.31	244.02	153.28	213.86	107.45	107.45	226.15

The predicted nominal purlin capacities are presented in Table 4. Capacities for Tests UB-P and 4PB-P assume restrained bending, and 4PB-NP tests assume unrestrained bending for predicting capacities. Distortional buckling controls the strength in most members; however, the local-global buckling mode is very close to the distortional load and sometimes controls, for example Specimen 19.

Table 4: DSM strength predictions.

Test Group	Purlin Label	Direct Strength Method Predictions							
		Global	Local		Distortional		Nominal	Controlling Mode	$M_{DSM,sys}$ (kip-in.)
		M_{ne} (kip-in.)	λ_ℓ	$M_{n\ell}$ (kip-in.)	λ_d	M_{nd} (kip-in.)	$M_{n,DSM}$ (kip-in.)		
UB-P Tests	24	153.32	0.82	148.15	1.12	151.53	148.15	(local-global)	147.44
	25-F^D	154.09	0.82	149.08	1.16	147.44	147.44	(distortional)	
	22-F	165.76	0.83	158.43	1.13	147.06	147.06	(distortional)	145.77
	23^D	161.72	0.83	154.54	1.21	145.77	145.77	(distortional)	
	12-F^D	139.41	0.78	138.98	1.18	140.28	138.98	(local-global)	138.98
	13	158.36	0.83	151.55	1.13	142.84	142.84	(distortional)	
4PB-P Tests	16-F^D	150.66	0.82	145.63	1.19	139.81	139.81	(distortional)	139.81
	14	150.11	0.81	145.67	1.12	145.88	145.67	(local-global)	
	19-F^D	164.56	0.80	160.89	1.10	144.35	144.35	(distortional)	144.35
	11	163.53	0.83	156.67	1.12	147.95	147.95	(distortional)	
	21-F^D	170.77	0.83	163.36	1.17	147.61	147.61	(distortional)	147.61
	7	164.99	0.82	158.99	1.13	150.22	150.22	(distortional)	
4PB-NP Tests	15-F^D	93.45	0.90	84.86	0.94	82.47	82.47	(distortional)	82.47
	8	100.79	0.95	88.32	0.98	83.89	83.89	(distortional)	
	10-F	91.38	0.90	83.43	0.94	81.40	81.40	(distortional)	81.22
	9^D	98.70	0.96	86.36	0.97	81.22	81.22	(distortional)	
	17-F	104.95	0.83	100.69	0.87	99.09	99.09	(distortional)	96.80
	18^D	109.33	0.87	101.88	0.89	96.80	96.80	(distortional)	
	32	104.87	0.97	90.81	0.99	85.70	85.70	(distortional)	80.70
	20-F^D	98.56	0.96	86.18	0.97	80.70	80.70	(distortional)	

Notes: 1. Purlin Label XX-F^D
D denotes the controlling specimen according to DSM
F denotes the specimen that controlled in testing

4. Test Results

The predicted capacity is presented using the Direct Strength Method (DSM), M_{DSM} in Table 5. The final predicted capacities for the purlin systems are notated as $M_{DSM,sys}$, which is the capacity of the controlling purlin. The capacities for the UB-P and 4PB-P tests are predicted using restrained properties contrary to the 4PB-NP tests, which assumed unrestrained bending.

Moment-midspan displacement system responses are presented in Figures 7 to 9. There is variation in the 4PB-NP tests, as they are affected by cross-section properties and imperfections, as there is no additional restraint or composite action with a panel present that could counteract some of the imperfections in the beam by providing bracing to the compression flange. Tests 4PB-NP-3 and 4PB-NP-4 had purlins in each test (Purlins 17, 18, and 32) with a higher yield stress and thickness compared to the other tests (reference Table 2 for section properties). This caused the system stiffness to increase as depicted by Plot in Figure 9. Also note that in Tests 4PB-P (Figure 8) and 4PB-NP (Figure 9), plots do not start at zero moment, as the weight of the loading frame (shown in Figure 5) induces a preload moment of 22 kip-in. into the purlins.

Table 5: Test results.

Test Group	Purlin Label	DSM Strength Predictions			Comparison		DSM Predicted-to-Tested Statistics	
		$M_{n,DSM}$ (kip-in.)	Controlling Mode	$M_{DSM,sys}$ (kip-in.)	M_{TEST} (kip-in.)	$M_{TEST}/M_{DSM,sys}$	Mean	COV
UB-P Tests	24	148.15	(local-global)	147.44	125.62	0.85	0.88	0.05
	25-F^{D}	147.44	(distortional)					
	22-F	147.06	(distortional)	145.77	124.71	0.86		
	23^{D}	145.77	(distortional)					
	12-F^{D}	138.98	(local-global)	138.98	129.72	0.93		
	13	142.84	(distortional)					
4PB-P Tests	16-F^{D}	139.81	(distortional)	139.81	148.70	1.06	1.03	0.04
	14	145.67	(local-global)					
	19-F^{D}	144.35	(distortional)	144.35	150.02	1.04		
	11	147.95	(distortional)					
	21-F^{D}	147.61	(distortional)	147.61	146.12	0.99		
	7	150.22	(distortional)					
4PB-NP Tests	15-F^{D}	82.47	(distortional)	82.47	94.59	1.15	1.23	0.07
	8	83.89	(distortional)					
	10-F	81.40	(distortional)	81.22	95.42	1.17		
	9^{D}	81.22	(distortional)					
	17-F	99.09	(distortional)	96.80	119.77	1.24		
	18^{D}	96.80	(distortional)					
	32	85.70	(distortional)	80.70	109.17	1.35		
	20-F^{D}	80.70	(distortional)					

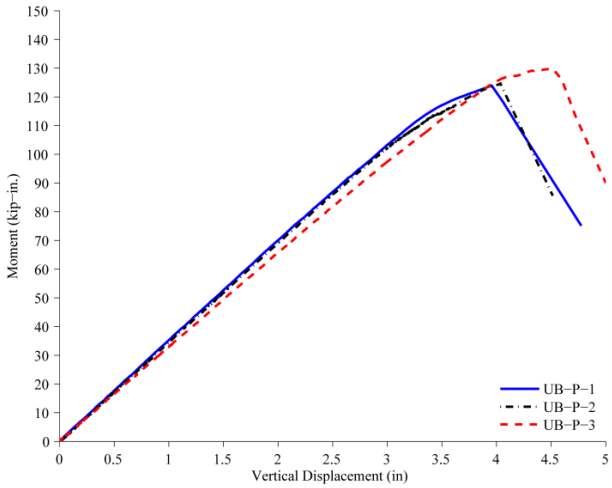

Figure 7: Moment-displacement response for downward pressure tests with sheathing (UB-P).

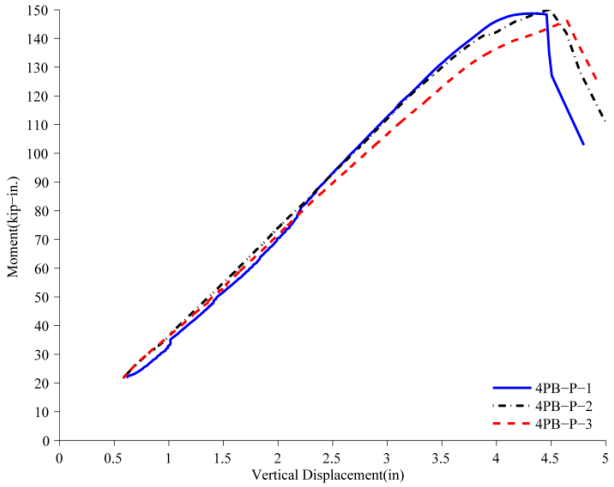

Figure 8: Moment-displacement response for downward pressure tests in four-point bending with panels.

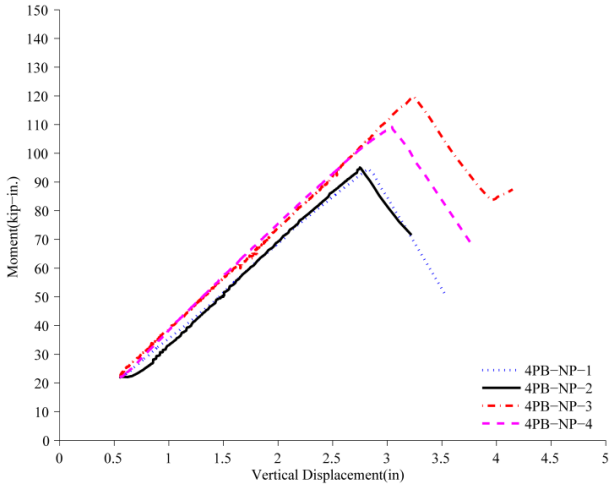

Figure 9: Moment-displacement response for downward pressure tests in four-point bending without panels.

5. Test Comparisons

5.1 Distortional buckling

Figures 10 through 12 present the distortional buckling results for the tests in this investigation. The failure mode changes between Tests UB-P/4PB-P and the 4PB-NP test. Whenever there was a panel present, distortional buckling and lateral-torsional buckling were not the governing failure modes, and local buckling controlled (Figure 10). However, when unrestrained (4PB-NP tests), the purlin was now controlled by primarily distortional buckling (Figure 11).

Measured distortional buckling data is presented in Figure 12. Some systems failed off center, which was caused by either uneven loading or imperfections in the purlins, which causes distortional half-waves to occur unevenly. The direction of the distortional half-waves should be noted as well. In the UB-P tests, the midspan half-wave at maximum moment always formed downward, whereas in the 4PB-P and 4PB-NP tests, the waves formed in both directions. Figure 12 presents the growth of distortional half-waves as loading increases. Only loading up to 80% of the failure moment is shown in Figure 12, as compression flange local buckling was picked up by the distortional LVDTs on Tests UB-P and 4PB-P. It is shown that a panel does provide some restraint to the compression flange. Comparing flange displacements (distortional buckling) at

80% of the failure load for the 4PB-NP to 4PB-P tests in Figure 12 confirm that the panel reduces distortional buckling deformation up to 50%. Distortional buckling deformation is reduced up to 75% until right before failure (80% M_{max}) when downward pressure exists with a panel (compare UB-P to 4PB-P flange displacements in Figure 12). Comparing UB-P to the other tests, it can be concluded downward pressure restrains distortional buckling up to until failure and causes the system to fail in an alternate failure mode.

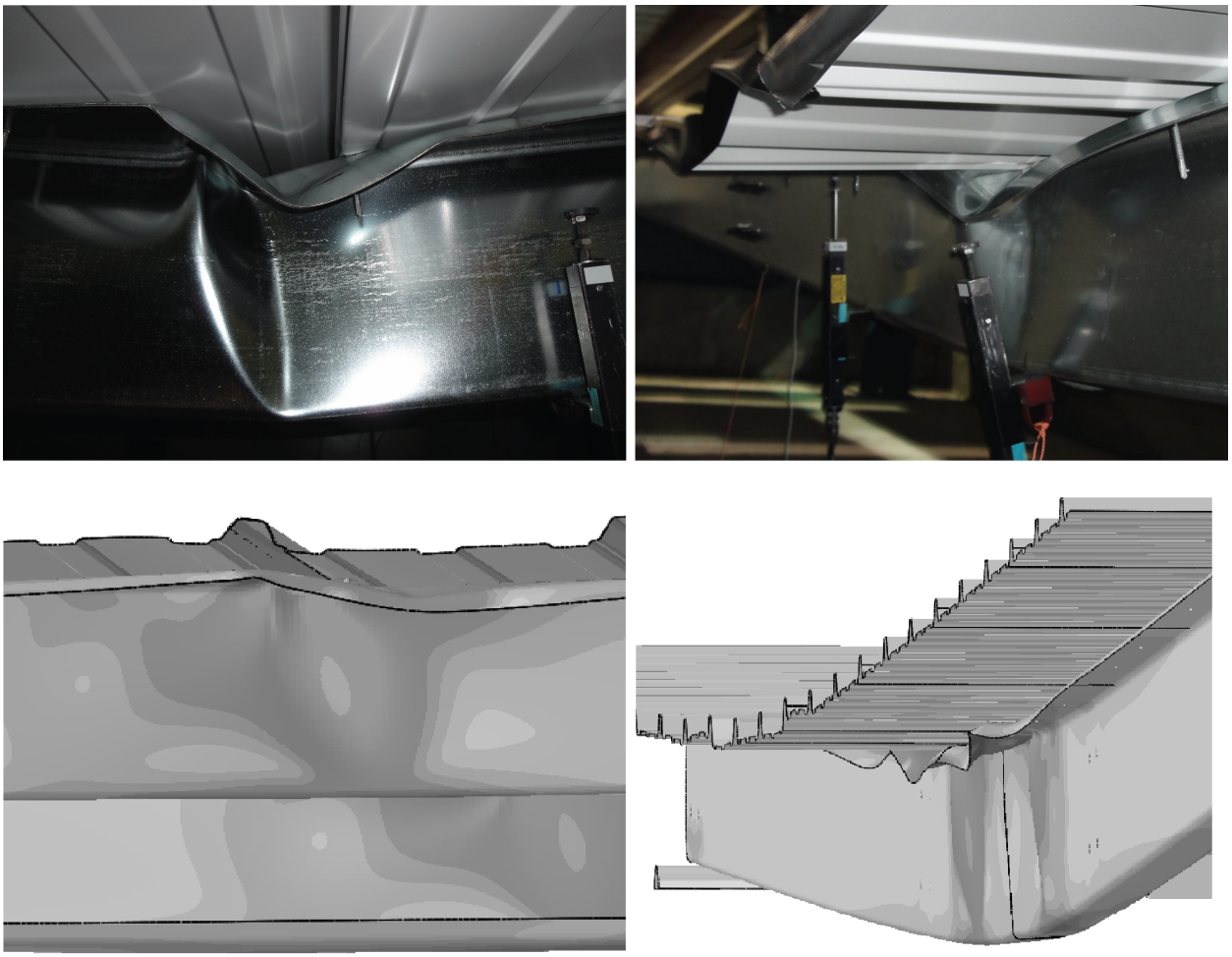

Figure 10: Failure mode UB-P and UB-P tests.

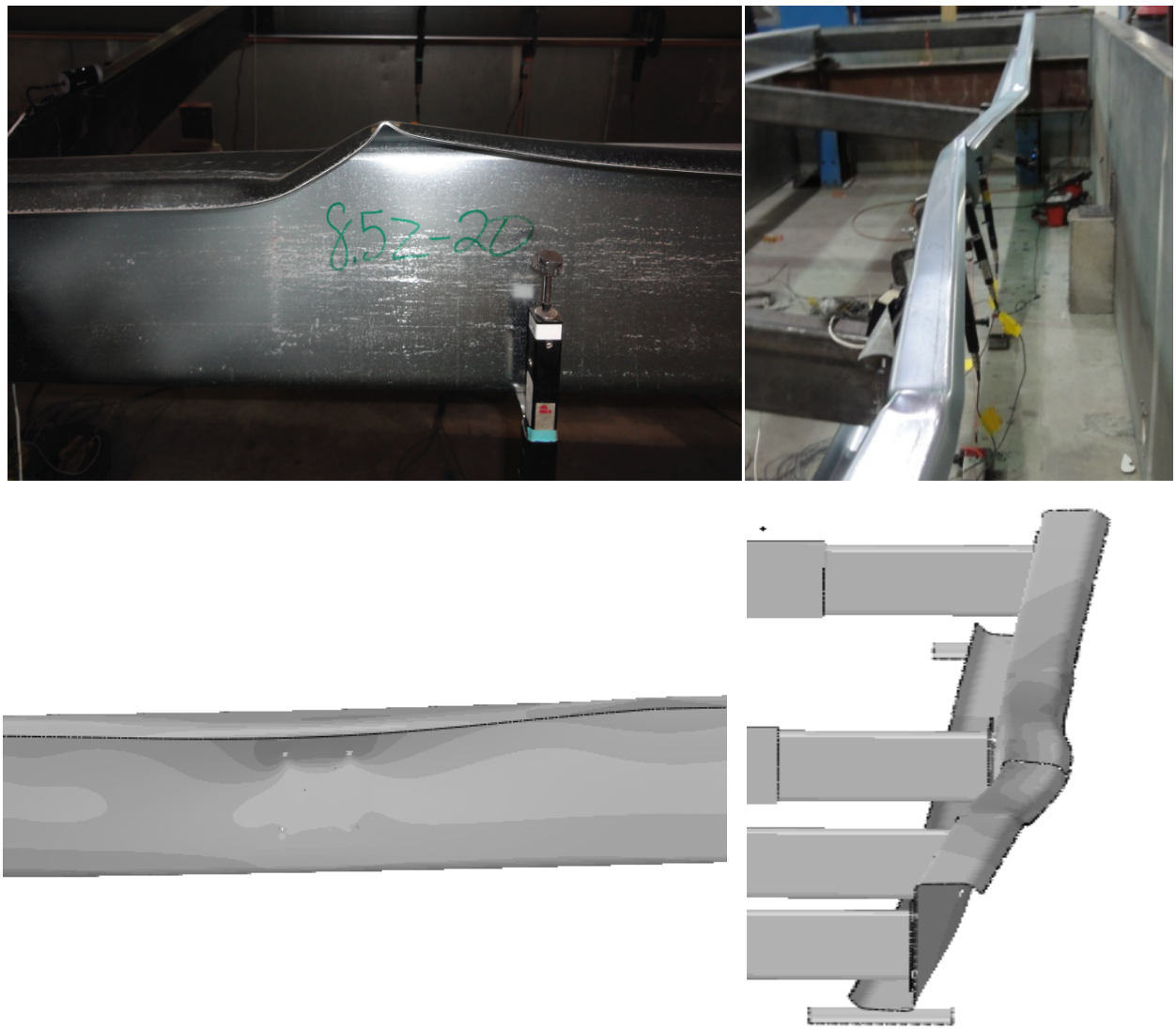

Figure 11: Failure mode 4PB-NP tests.

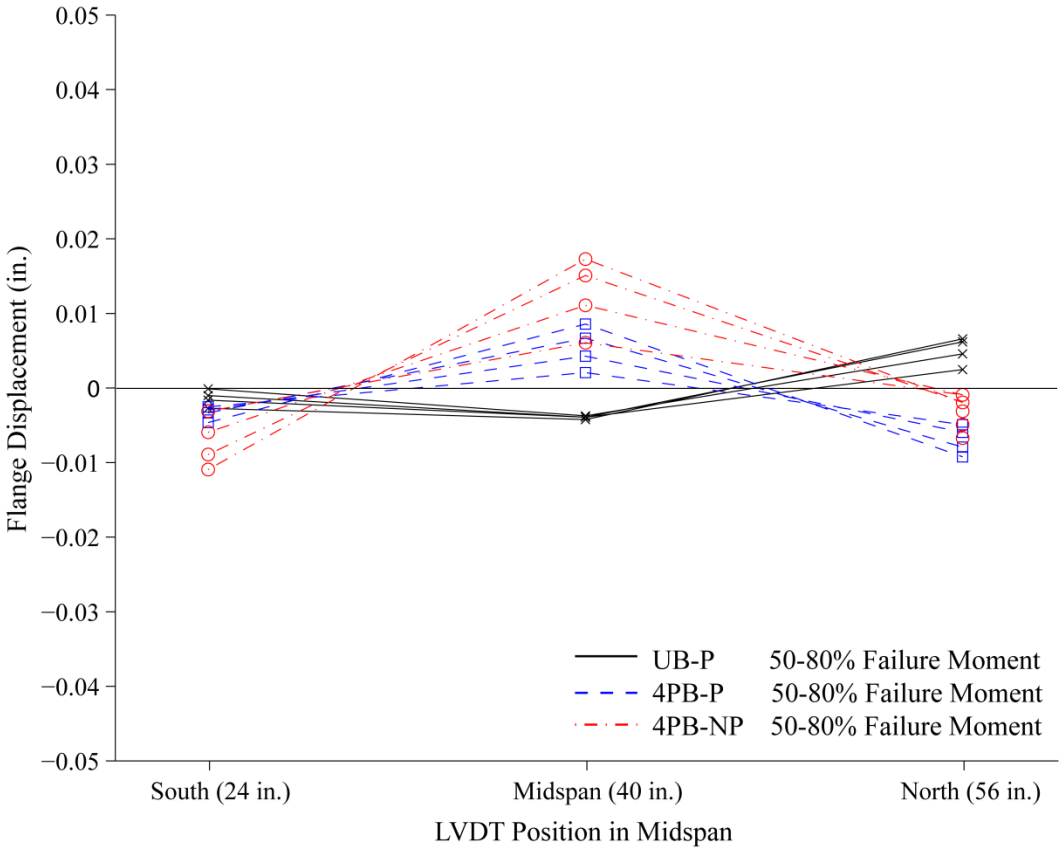

Figure 12: Typical distortional displacement responses comparison.

5.2 Moment capacity

Figure 13 provides a comparison of the moment capacities of all three test types. There is on average a 30% increase in capacity when a panel is added to the system (compare 4PB-NP to 4PB-P tests in Figure 13 or M_{TEST} values in Table 5). This also confirms that restrained bending can be assumed in the prediction methods to determine elastic buckling parameters. A comparison of Tests 4PB-P to UB-P in Table 5 shows that when uniform pressure exists, overall moment capacity decreases by an average 12%. It is hypothesized that increased bending in the flange occurs due to the loading conditions. Because the pressure loads the entire flange instead of just over the web as in four-point bending tests, moment develops around the web-flange junction, creating a deformation (imperfection) as shown in Figure 14. With this deformation present, the effective moment of inertia decreases, causing the moment capacity of the purlin to decrease as well. Another possibility is that because the panels were not continuous transversely in the tests, panel deformations were higher than what would be in a typical roof system, and these deformations pushed down the purlin flanges, causing premature failure. Finite element modeling to collapse is presented later in this paper to study purlin deformation in closer detail.

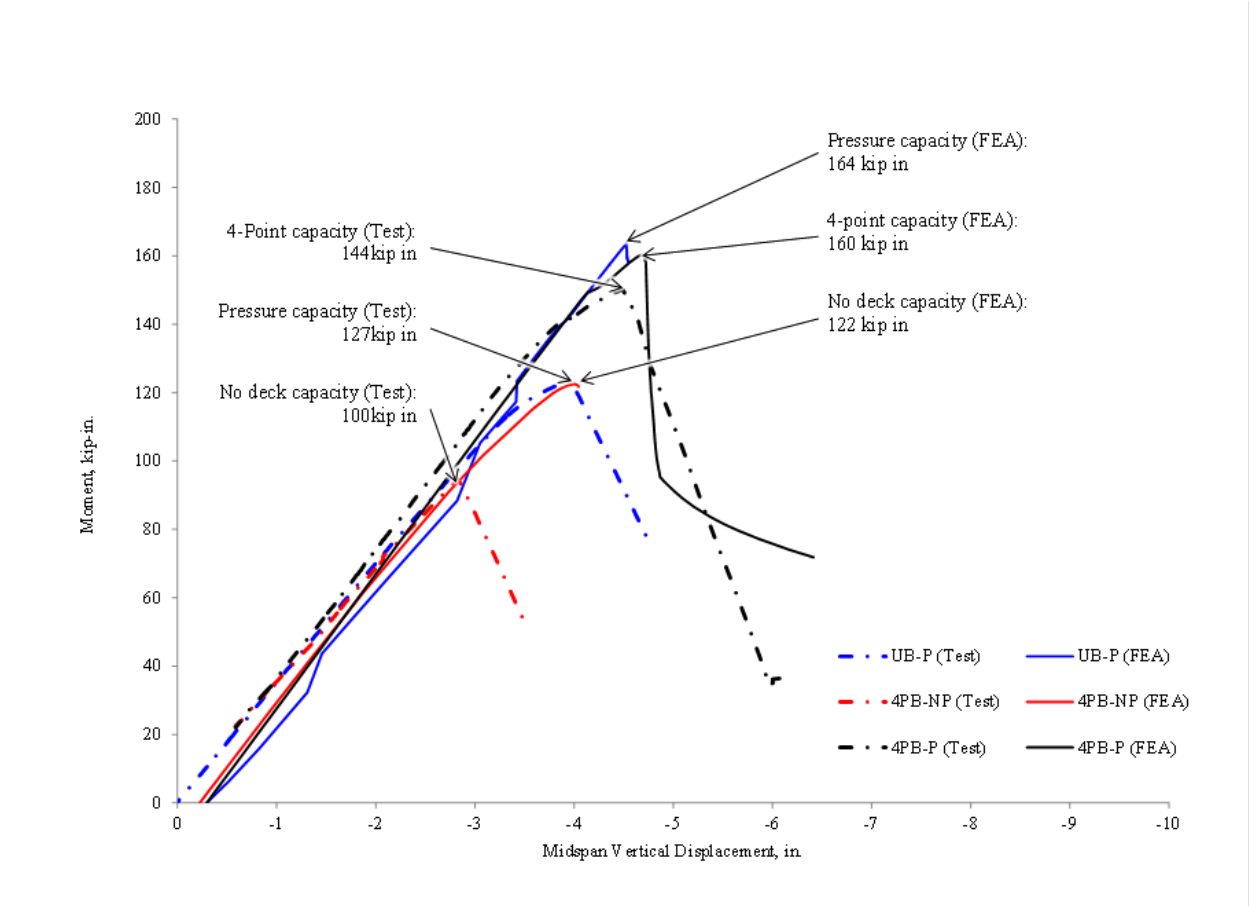

Figure 13: Force-displacement responses – all groups.

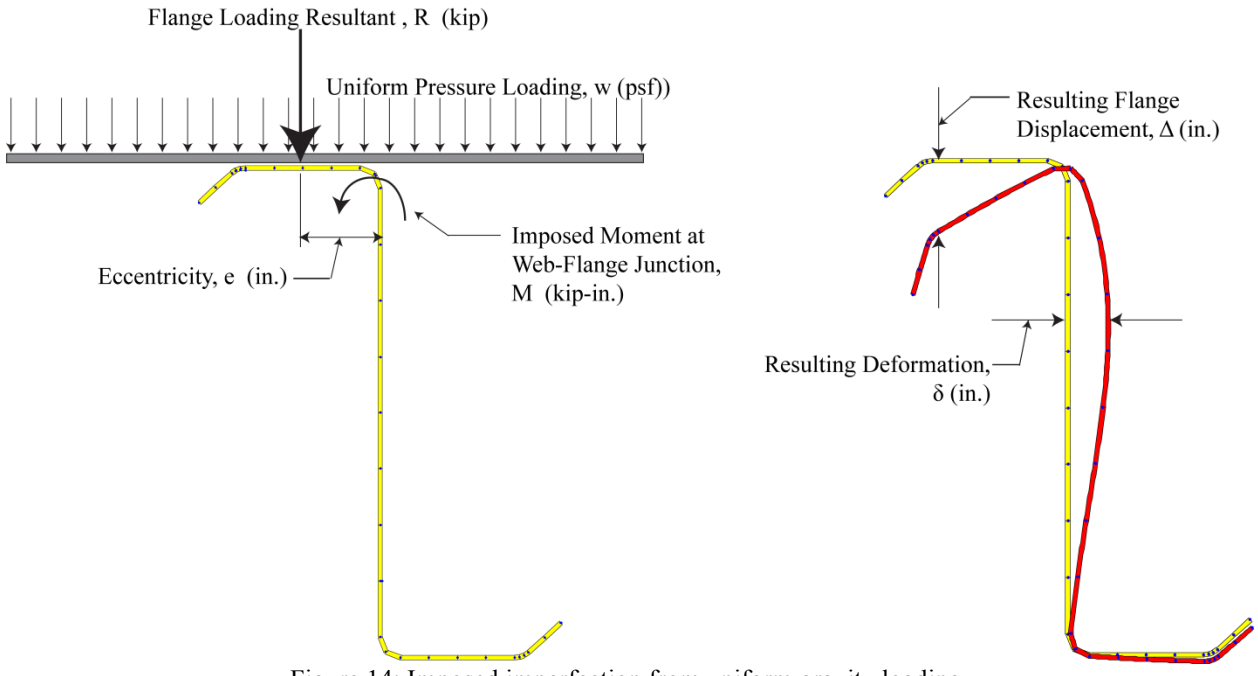

Figure 14: Imposed imperfection from uniform gravity loading

6. Finite Element Modeling

A finite element (FE) model of the three test configurations was developed in the commercial FE software ABAQUS v6.12-1. Figure 15 shows the model geometry, including the purlin, deck, bracing beams, and roller support. The models represent one-quarter of the test apparatus with boundary conditions applied as follows: symmetric boundary conditions applied on the purlin at midspan, on the braces at their midspan, and on the two edges of the roof deck as indicated in Figure 15; the long edges of the roller are pinned.

Large deformations and material nonlinearity are included; the roof deck and purlin material definitions are linear-elastic-perfectly-plastic, with a deck yield strength of 50 ksi. Purlin yield strength is 73 ksi based on coupon tests of the purlins tested. Cold bending residual stresses and plastic strains are not considered.

The roof deck is modeled with panels approximately 3 ft wide, and the first and last ribs of each panel overlap. The roof deck is modeled with four-node linear general-purpose shell element S4. Contact with friction is included between the panels of the roof deck, between the roof deck and the purlin, between the brace endplates and the purlin web, and between the purlin and the roller support. The roof panels are also connected to the top flange of the purlin with beam elements simulating the screws at 12 in. o.c. and are connected to each other with similar beam elements at the lapped ribs.

The purlin is modeled with four-node linear general-purpose shell element S4. The purlin mesh is seeded with geometric imperfections developed from a buckling load analysis of the roof structure under uniform pressure. The imperfections are determined from the first global, distortional, and web local buckling modes. The mode shapes were scaled to have a peak magnitude based on the values published by Shafer and Peköz (1999). We select a peak magnitude of $(\mu + 1\sigma)t$ from their measurements for the distortional and web local buckling modes – 2.36t and 1.16t, respectively – and a peak magnitude of 3.54t for the global buckling mode.

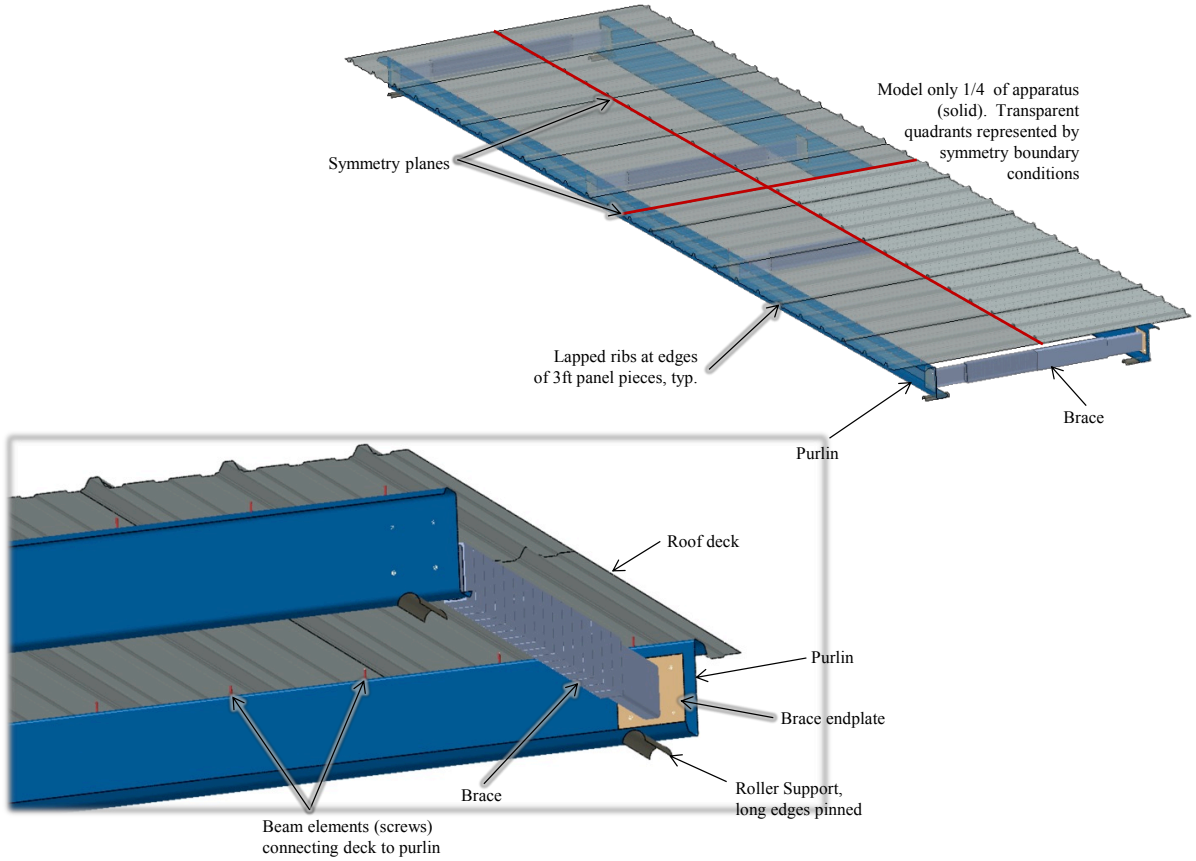

Figure 15: Finite element model showing the purlin, deck, bracing beams, and roller support.

The models simulate the response of the roof structure for the three loading types tested. Figure 13 shows the load-displacement response predicted by the model plotted against the measured response from tests. All three loading cases have a linear load-displacement response up to about 90% of the failure load. Additional analyses (not shown) of an ideal purlin geometry without imperfections found linear load-displacement response up to failure. The imperfections then have a minimal effect on system stiffness while improving convergence numerical conditioning of the model. Failure loads are 2% – 4% lower with imperfections included for the models with the roof deck included. For the model with no roof deck, the magnitude of imperfections significantly affects capacity, as discussed later.

The predicted model stiffness does not change across the three configurations, whereas during testing, the addition of the deck increased system stiffness. Therefore, it can be concluded that the finite element model may not be incorporating interaction between the deck and the purlin accurately.

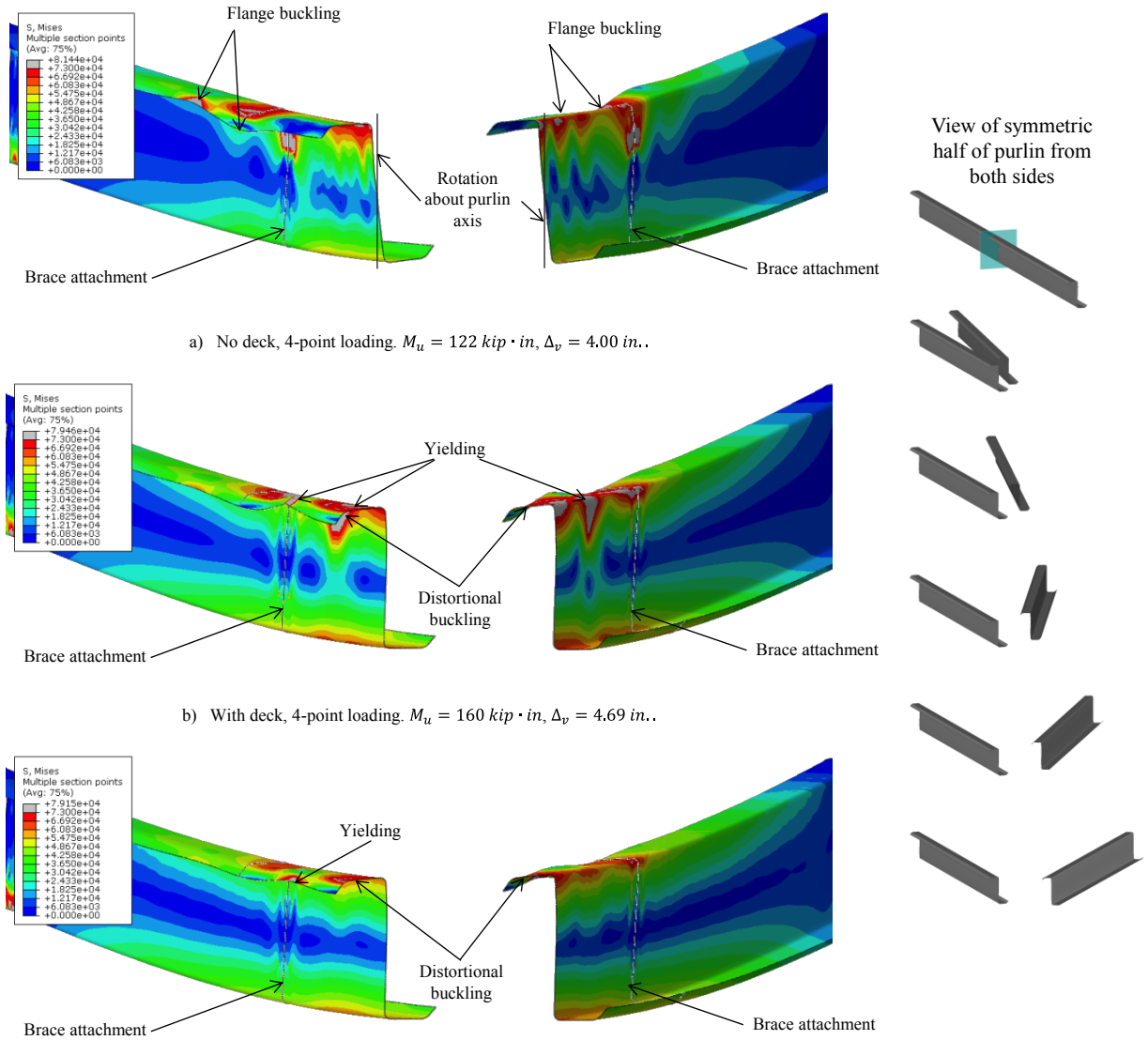

Figure 16: Deformed shape and von Mises stress [psi] on top and bottom surfaces at ultimate load looking at the symmetry plane at midspan. Contour limit set at F_y = 73 ksi. No displacement magnification.

The stiffness of the system, measured as the slope of the curve of midspan moment versus midspan vertical displacement, is approximately k_{FE} = 40 kip-in./in. for all three configurations, indicating that the roof deck has little effect on system stiffness. Physical tests found stiffnesses between k_{test} = 32 and 39 kip-in./in.

The models show that, as with the physical tests, the presence of the roof deck increases the failure load – the peak bending moment increases from 122 to 160 kip-in. under four-point loading. Contrary to the results of physical testing, the model predicts that the pressure loading case has a higher failure load than the four-point loading case when the roof deck is present – 164 versus 160 kip-in. Physical tests measured a capacity of 127 kip-in. under pressure loading.

The disparity in capacities between the tests and model under pressure loading could be due to differences in the load application; the model applies a uniform pressure over the exposed area of the roof deck, while in tests, a pressure difference was applied across a plastic sheet draped over the apparatus and falling over the sides of the deck, which may have introduced incidental loads to the system.

The deformed shapes at capacity are shown in Figure 16Figure 16 for the three configurations, ordered by increasing capacity as predicted by the FE model. The contours show the von Mises stress [psi] on the top and bottom surfaces of the purlin, with stresses above the yield strength F_y = 73 ksi shown in grey:

- Figure 16 a), the configuration with no deck under four-point loading, shows buckling of the compression flange on the far side of the brace (from the midspan) and rotation of the purlin about its axis in a lateral-torsional mode. The capacity is M_u = 122 kip-in.
- Figure 16 b), the configuration with the roof deck under four-point loading, shows distortional buckling of compression flange at midspan and yielding at the intersection of the web and the compression flange. The capacity is M_u = 160 kip-in.
- Figure 16 c), the configuration with the roof deck under uniform pressure loading, shows distortional buckling of the compression flange at midspan and yielding at the edge of the top flange just inboard the brace towards midspan. The capacity is M_u = 164 kip-in.

The deformed shape for four-point loadings with and without the roof deck at the termination of the analysis is shown next to the tested failed purlins in Figures 10 and 11. The plots show the failure mechanism more clearly. Both tests and models with the roof deck attached showed that the most-significant deformation of the compression flange occurred at a screw connecting the deck to the purlin. With no roof deck, both tests and models show lateral-torsional buckling failures.

It appears that the pressurized roof deck restrains the upward displacement of the compression flange, as shown in the contact pressure distributions in Figure 17. The contour under uniform pressure also shows more contact points from the deck above on the right side (i.e., the side where the deck spans between the two purlins) than does the contour under four-point loading, confirming that the panel transfers load to the purlin through contact. It is interesting to note how few points of contact exist between the deck and the purlin because of the corrugated shape of the deck panels. Figure 18shows the vertical displacement of the top flange along the length of the purlin. While the magnitudes are much larger than those measured during tests (see Figure 13), the plot does show that for uniform pressure, the flange is restrained and does not displace upwards, while for other configurations, the flange displaces both upwards and downwards. Note that under four-point loading, the flange at midspan initially displaces upwards before moving rapidly downwards approaching the ultimate moment capacity.

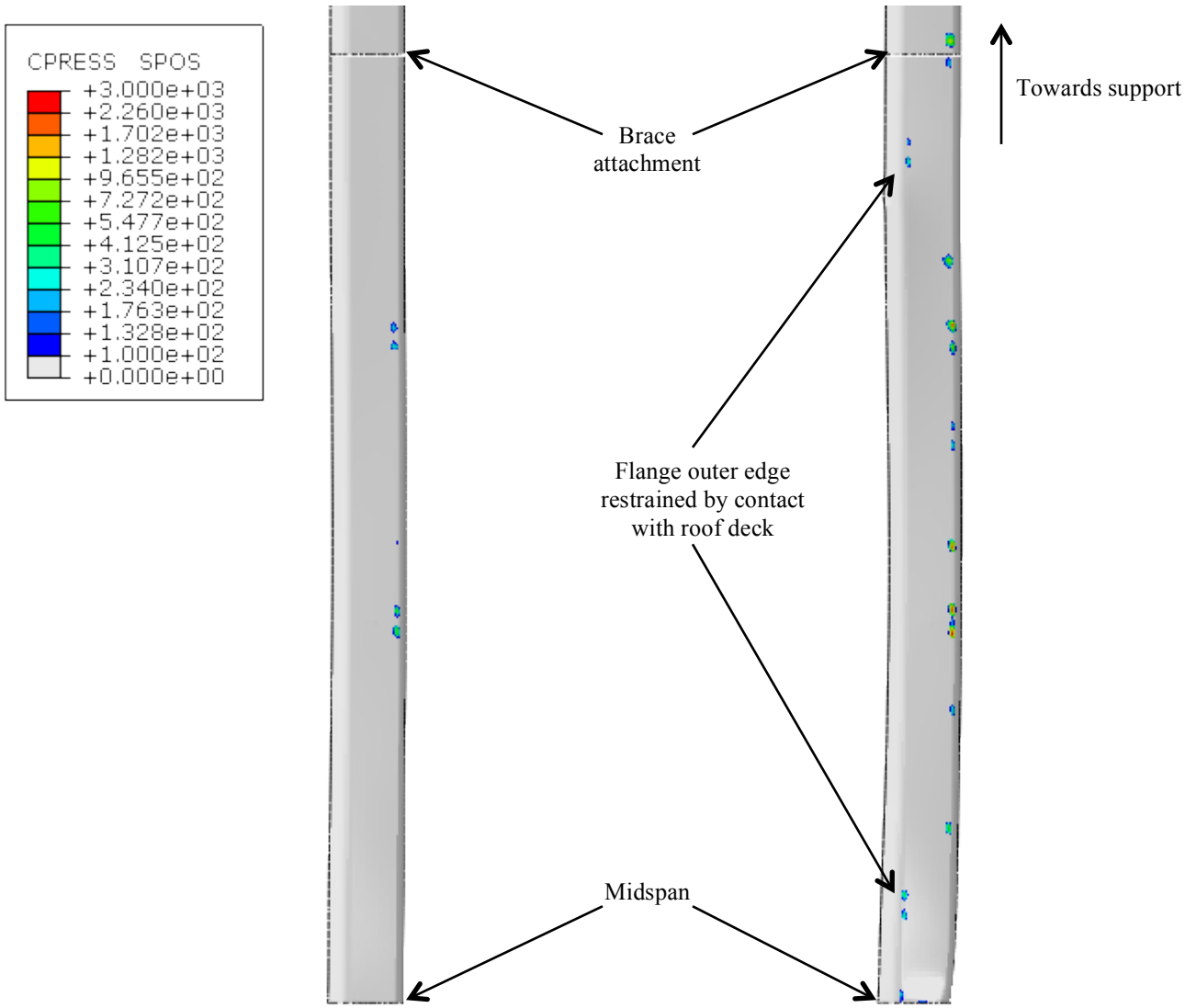

Figure 17: Contact pressure [psi] for four-point (left) and uniform pressure (right) loading conditions.

The purlin cross-section at midspan is shown in Figure 19. The figure confirms the failure modes discussed with Figure 16; without the roof deck, the purlin fails in a global lateral-torsional buckling mode, and in both configurations with the roof deck, the purlin fails in a distortional buckling mode. Note that these profiles are plotted at midspan while the largest cross-section deformation may occur at another location, as is clearly the case for the four-point bending test with the roof deck shown in Figure 16b. As mentioned earlier, the magnitude of imperfections had little effect on the ultimate moment capacity of the configurations with the roof deck attached to the purlin. By contrast, the magnitude of imperfections had a significant effect on the capacity of the purlin with no roof deck present. Figure 20Figure shows the moment-displacement curves for different imperfection magnitudes for the configuration with no roof deck and also the data measured from tests. The tested capacity is 95 kip-in. Capacities determined from the FE models range from 107 kip-in. for the largest imperfection considered to 146 kip-in. with no imperfections or from 13% to 54% higher than the tested capacity.

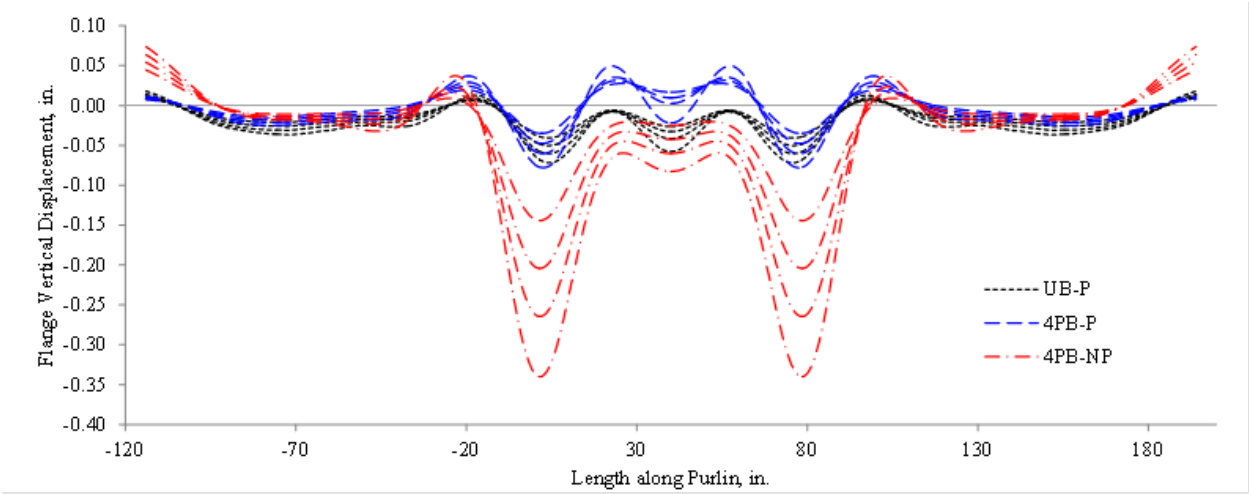

Figure 18: Flange vertical displacement along the purlin. The ordinate is set with zero at the fist brace point, compatible with Figure12. The traces for each loading condition show the deformed shape at 50%, 60%, 70%, and 80% of the ultimate moment capacity.

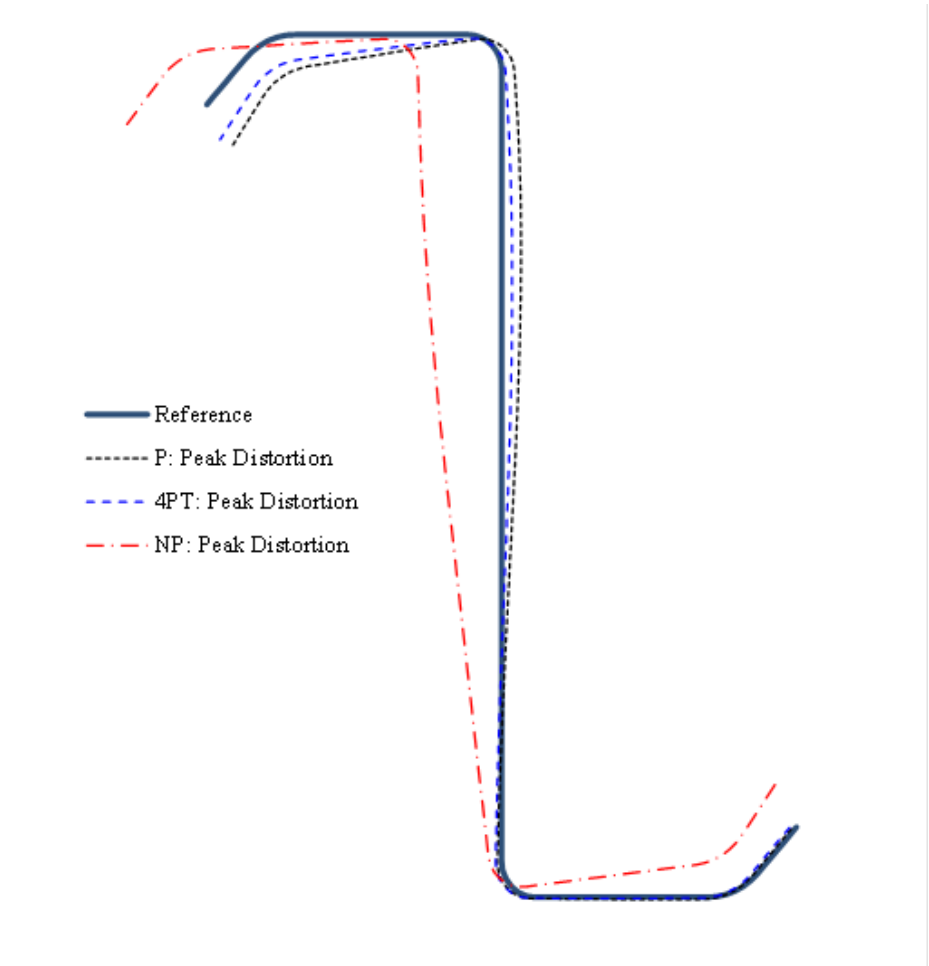

Figure 19: Purlin cross-section at midspan at the time in the simulation where the highest deformation/displacement of the cross-section occurs – no displacement magnification.

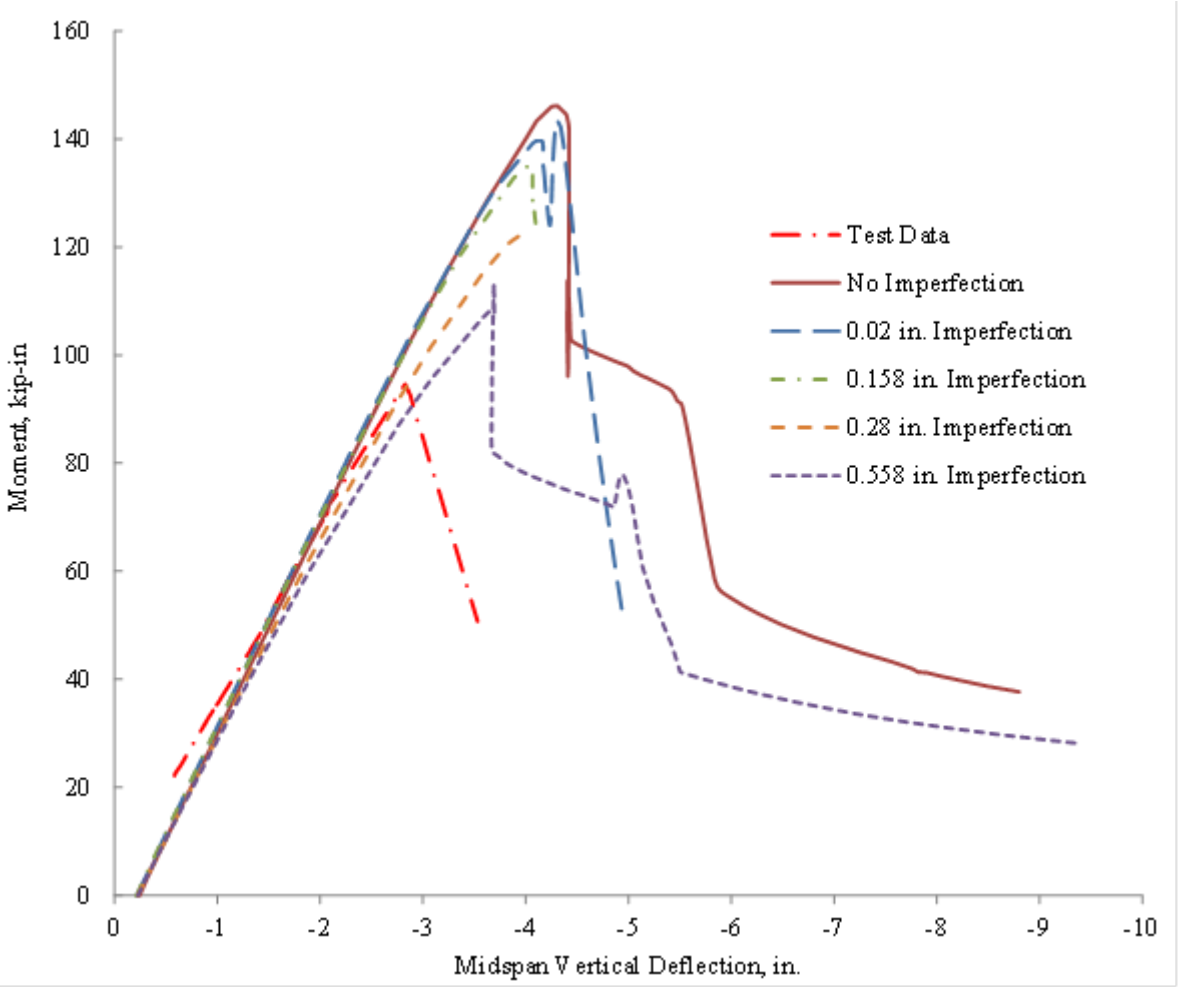

Figure 20: Moment-deflection curves for the configuration with no roof deck for several imperfection magnitudes.

7. Conclusions

The influence of through-fastened panels and downward (gravity) pressure were studied both with pressure chamber tests and finite element simulations to collapse. The presence of through-fastened panels increased the system capacity and the application of downward pressure prevented upward distortional buckling deformation in the compression flange. Downward pressure was shown in the tests to decrease capacity relative to four-point bending, which is inconsistent with intuition and with the finite element simulations to collapse. It is hypothesized that lack of transverse panel continuity in the tests resulted in large panel deformations that forced the purlin flanges down, causing premature system failure. Also, it is possible that the draped plastic sheeting in the downward pressure test introduced additional forces at the edge of the panel overhang that could cause the purlin to fail earlier than expected. As this investigation is based on a small number of tests, future research is needed to determine whether this reduction in capacity exists. Additional testing and finite modeling research is recommended to determine whether the decreased moment capacity under uniform pressure is isolated to testing in this investigation or occurs in a multipurlin roof system by either supporting the overhung panel or setting up a multispan system for testing.

Although a decrease in capacity was measured in tests, distortional buckling of cold-formed steel purlins with compression flange bracing subjected to downward pressure in a metal building roof system is significantly reduced. Tests have shown that compression flange displacements can be restrained by up to 75% of the unrestrained distortional buckling. Including the rotational stiffness provided by a restraining element (e.g., brace, panel, and sheathing), k_ϕ in CUFSM would predict the distortional buckling moment at a greater accuracy.

The analysis showed that the capacity of a purlin without an attached roof deck is highly sensitive to geometric imperfections. A study of imperfections present in as-shipped purlins and their effect on capacity is recommended given the sensitivity to imperfections of the capacity of a purlin without a roof deck predicted by analysis.

8. References

AISI-S100 (2007). *North American Specification for the Design of Cold-Formed Steel Structural Members*. Washington, D.C., American Iron and Steel Institute.

AISI-TS (2007). "S908-08 Base Test Method for Purlins Supporting a Standing Seam Roof System." *Test Standards for Use with the North American Cold-Formed Steel Specification*. Washington, D.C., American Iron and Steel Institute.

ASTM (2005). *A370-05, Standard Test Methods and Definitions for Mechanical Testing of Steel Products*. West Conshohocken, PA. ASTM International.

DSM (2006) American Iron and Steel Institute (2006), Direct Strength Method (DSM) Design Guide, Design Guide CF06-1, Washington, DC, June 2006.

Schafer, B.W. and S. Ádány (2006). "Buckling Analysis of Cold-Formed Steel Members using CUFSM: Conventional and Constrained Finite Strip Methods." *Eighteenth International Specialty Conference on Cold-Formed Steel Structures*. Orlando, FL.

Schafer, B.W., Sangree,R.H., Guan Y. (2008). "Rotational Restraint of Distortional Buckling in Cold-Formed Steel Framing Systems." *Fifth International Conference on Thin-Walled Structures*. Brisbane, Australia.

Schafer, B.W., and T. Pekoz (1999). "Laterally Braced Cold-Formed Steel Flexural Members with Edge Stiffened Flanges." *Journal of Structural Engineering*. ASCE, Vol. 125 No. 2, February 1999.